MATERIALS SCIENCE

Fast constructing polarity-switchable zinc-bromine microbatteries with high areal energy density

Chunlong Dai[1], Linyu Hu[1], Xuting Jin[1], Ying Wang[1], Rui Wang[2], Yukun Xiao[3], Xiangyang Li[1], Xinqun Zhang[1], Li Song[1], Yuyang Han[1], Huhu Cheng[4], Yang Zhao[1], Zhipan Zhang[1]*, Feng Liu[5]*, Lan Jiang[6], Liangti Qu[4]*

Microbatteries (MBs) are promising candidates to provide power for various miniaturized electronic devices, yet they generally suffer from complicated fabrication procedures and low areal energy density. Besides, all cathodes of current MBs are solid state, and the trade-off between areal capacity and reaction kinetics restricts their wide applications. Here, we propose a dual-plating strategy to facilely prepare zinc-bromine MBs (Zn-Br_2 MBs) with a liquid cathode to achieve both high areal energy density and fast kinetics simultaneously. The Zn-Br_2 MBs deliver a record high areal energy density of 3.6 mWh cm^{-2}, almost an order of magnitude higher than available planar MBs. Meanwhile, they show a polarity-switchable feature to tolerate confusion of cathode and anode. This strategy could also be extended to other battery systems, such as Zn-I_2 and Zn-MnO_2 MBs. This work not only proposes an effective construction method for MBs but also enriches categories of microscale energy storage devices.

INTRODUCTION

Microscale energy storage devices have attracted increasing research interests due to their potential applications in various miniaturized electronics, such as microrobots, implantable medical devices, and Internet of Things (*1*–*3*). To date, micro-supercapacitors (MSCs) have been extensively studied due to high power density and ease of fabrication, as their two electrodes could be the same materials (*4*–*10*). However, the low energy density, fast self-discharge, and unstable voltage output limit their practical applications (*11*–*13*). Microbatteries (MBs) could effectively overcome these challenges (*14*).

Although substantial progresses have been made in recent years, current planar MBs still suffer from tedious and complicated construction procedures as it is a considerable challenge to prepare and match cathode and anode at a microscale (*15*–*23*). For example, a multistep mask-assisted filtration strategy was proposed to construct a planar sodium-ion MB, which required at least six procedures (*24*), including preparation of cathode and anode active materials, and then step by step build current collector, cathode, and anode on the nylon substrate with the help of a preprepared interdigitated mask, adding the gel electrolyte for the final encapsulation. Besides, current planar MBs are limited to solid cathodes and generally deliver unsatisfactory areal capacity and energy density (most are lower than 300 μAh cm^{-2} and 500 μWh cm^{-2}) due to inferior power density originated from a too thick solid electrode (*25*–*28*). Furthermore, current MBs contain an excess amount of anode (typically more than 10 times than the cathode), which results in a decreased overall performance and is not applicable in practice.

Here, we propose a dual-plating strategy to fast construct zinc-bromine (Zn-Br_2) MBs with a liquid cathode, which not only gets rid of the complicated and time-consuming procedures of traditional methods but also helps the planar MB access high areal energy density and power density. The electrolyte is the key point, and it contains redox-active cations (Zn^{2+}) and anions (Br^-). During the charging process, Zn^{2+} gain electrons and then get deposited on the negative current collector to form the zinc anode; concomitantly, Br^- loss electrons to generate Br_2 that work as the cathode on the positive current collector. The Br_2 cathode and the Zn anode return to soluble Br^- and Zn^{2+}, respectively, during the discharging process (*29*). The cathode and anode are generated one by one, and no one electrode is excessive, enabling the maximization of the overall electrochemical performance. The dual-plating and stripping reactions are as follows

$$\text{Cathode: } 2\,Br^- - 2\,e^- \leftrightarrow Br_2\ E_0 = 1.06\ \text{V versus SHE} \quad (1)$$

$$\text{Anode: } Zn^{2+} + 2\,e^- \leftrightarrow Zn\ E_0 = -0.76\ \text{V versus SHE} \quad (2)$$

The Zn-Br_2 MBs shows an electrode-less feature, and it only requires an interdigitated current collector and a redox-active electrolyte, eliminating the synthesis of active materials, which is a necessary procedure for previous MBs. It also bypasses the challenge of precisely coat or deposit cathode and anode on different microelectrodes. Moreover, the troublesome and time-consuming mass matching of the cathode and anode procedure could also be ingeniously avoided, because they always generate one by one (*30*). It is worth mentioning that, to the best of our knowledge, the Zn-Br_2 system have not yet been introduced into the field of microscale energy storage, because it is hard to manipulate liquid Br_2 through previous methods. The new MB is expected to achieve high energy density and power density at the same time due to the liquid nature of the

[1]Key Laboratory of Cluster Science, Ministry of Education, Beijing Key Laboratory of Photoelectronic/Electrophotonic Conversion Materials, School of Chemistry and Chemical Engineering, Beijing Institute of Technology, Beijing 100081, P. R. China. [2]Key Laboratory for Advanced Materials and Joint International Research Laboratory of Precision Chemistry and Molecular Engineering, Feringa Nobel Prize Scientist Joint Research Center, Frontiers Science Center for Materiobiology and Dynamic Chemistry, Institute of Fine Chemicals, School of Chemistry and Molecular Engineering, East China University of Science and Technology, Shanghai 200237, P. R. China. [3]Joint School of National University of Singapore and Tianjin University, International Campus of Tianjin University, Binhai New City, Fuzhou 350207, China. [4]Key Laboratory of Organic Optoelectronics and Molecular Engineering of Ministry of Education, Department of Chemistry, Tsinghua University, 100084 Beijing, P. R. China. [5]State Key Laboratory of Nonlinear Mechanics, Institute of Mechanics, Chinese Academy of Sciences, Beijing 100190, P. R. China. [6]Laser Micro/Nano-Fabrication Laboratory, School of Mechanical Engineering, Beijing Institute of Technology, Beijing 100081, P. R. China.
*Corresponding author. Email: zhipan@bit.edu.cn (Z.Z.); liufeng@imech.ac.cn (F.L.); lqu@mail.tsinghua.edu.cn (L.Q.)

Br_2 cathode. For traditional MBs, increasing areal loading to pursue higher energy density could result in long ion transfer distance in solid active materials and lead to decreased power density. The liquid feature of the Br_2 cathode could circumvent the trade-off between energy density and power density due to fast reaction kinetics in the liquid medium. Benefiting from these merits, the Zn-Br_2 MBs deliver record high areal capacity and areal energy density (2220 μAh cm^{-2} and 3645 μWh cm^{-2}) and maintain an excellent power density of 26.2 mW cm^{-2} (even better than most MSCs). It is worth mentioning that these electrochemical performances are obtained without any excess of cathode or anode. They also have good flexibility, maintaining almost the same galvanostatic charge-discharge (GCD) curves under different bending states. Meanwhile, the Zn-Br_2 MBs show a unique feature of switchable polarity, allowing self-rectification on possible faulty operations such as wrongly connecting cathode and anode during charging. This work provides a new simple but efficient method to fast construct in-plane MBs, which is applicable for both solid and liquid microelectrodes. The Zn-Br_2 MB as a novel MB not only enriches the microscale energy storage devices but also sets a new benchmark for in-plane MBs.

RESULTS

Construction of Zn-Br_2 MBs

The preparation of Zn-Br_2 MBs is shown in Fig. 1A. A flexible and hydrophilic carbon nanotube (CNT) paper (about 10 μm in thickness) is first stuck on the insulating tape (fig. S1) and then patterned into interdigitated electrodes (the area is about 0.18 cm^2 based on all fingers and gaps) through the laser carving method. The microelectrode is flexible and could be easily integrated (Fig. 1B). The Zn-Br_2 MBs are obtained after covering a redox-active gel electrolyte containing Br^- and Zn^{2+} on the interdigitated electrodes. The prepared Zn-Br_2 MBs are at the discharging state. Once a bias (1.85 V is used here) is applied, the Br_2 and Zn could be in situ plated on the CNT microelectrodes to act as the cathode and anode (Fig. 1C), respectively, and then to provide power for miniaturized electronics.

Choice of electrolyte

The redox-active electrolytes greatly affect the electrochemical performance of the Zn-Br_2 MBs (Fig. 2, A to C). The composition of the redox-active electrolyte is first optimized through a homemade cell (fig. S2). When $ZnBr_2$ is used as the Zn and Br sources, the Zn-Br_2 battery delivers a low Coulombic efficiency of about 40% due to the diffusion of soluble Br_3^- spontaneously formed from Br_2 and Br^- during the charging process (Fig. 2D and fig. S3) (*31*–*33*), and its diffusion process can be witnessed by the slow percolation of light yellow colored Br_3^- into the electrolyte (fig. S4). Tetrabutylammonium bromide (TBABr; $C_{16}H_{36}BrN$) has been reported as an efficient complexing agent for Br_3^- to impede the cross-diffusion of Br_3^- (*33*). When TBABr is selected as the Br source and $ZnSO_4$ is used as the Zn source in the electrolyte to construct the Zn-Br_2 MBs, the Coulombic efficiency of MBs is improved to 78% (Fig. 2E), but the polarization between charging and discharging processes substantially increases to 822 mV, suggesting the slow reaction kinetics of solid $TBABr_3$ complex (fig. S5).

Instead, 1-methyl-3-propylimidazolium bromide (MPIBr; $C_7H_{13}BrN_2$) is found to provide high Coulombic efficiency and fast reaction kinetics at the same time. MPIBr is an ionic liquid composed of MPI^+ cation and Br^- anion, and its molecular structure is shown in fig. S6. The device prepared with a 1 M MPIBr + 1 M $ZnSO_4$ electrolyte shows a high Coulombic efficiency of 99% and a low polarization of 144 mV (Fig. 2, F and G). The Raman spectra, ultraviolet-visible (UV-vis) spectra, ^1H nuclear magnetic resonance (NMR) spectra, ^{13}C NMR spectra, and electrospray ionization mass spectrometry spectra indicate that the $MPIBr_3$ liquid cathode is formed during the charging process (figs. S7 to S10). The Zn anode is also generated at the same time (fig. S11). The UV-vis spectra were used to detect the Br_3^- in the electrolyte. During the charging process, a strong Br_3^- signal is found in the $ZnBr_2$ electrolyte (Fig. 2H), but there is no obvious signal of Br_3^- in the electrolyte containing MPIBr and $ZnSO_4$ (Fig. 2I and fig. S12), further demonstrating that MPI^+ could effectively complex with Br_3^- ($MPI^+ + Br_3^- \rightarrow MPIBr_3$). When MPIBr or TBABr is added to a solution containing Br_3^- (fig. S13),

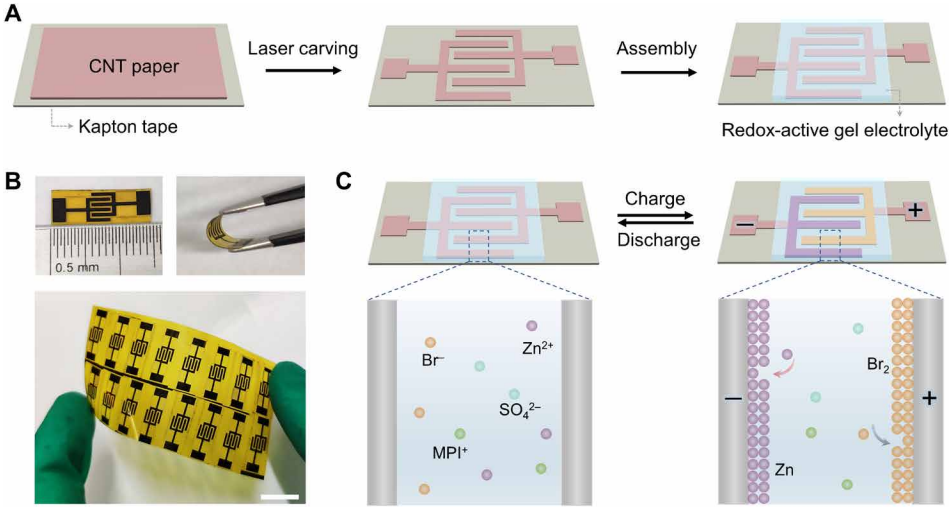

Fig. 1. Construction process and working mechanism of the Zn-Br_2 MBs. (**A**) Fabrication process of the Zn-Br_2 MBs. (**B**) Digital photographs of flexible Zn-Br_2 MBs at flat and bending states. Scale bar, 1 cm. (**C**) In situ construction of Br_2 cathode and Zn anode during the charging process.

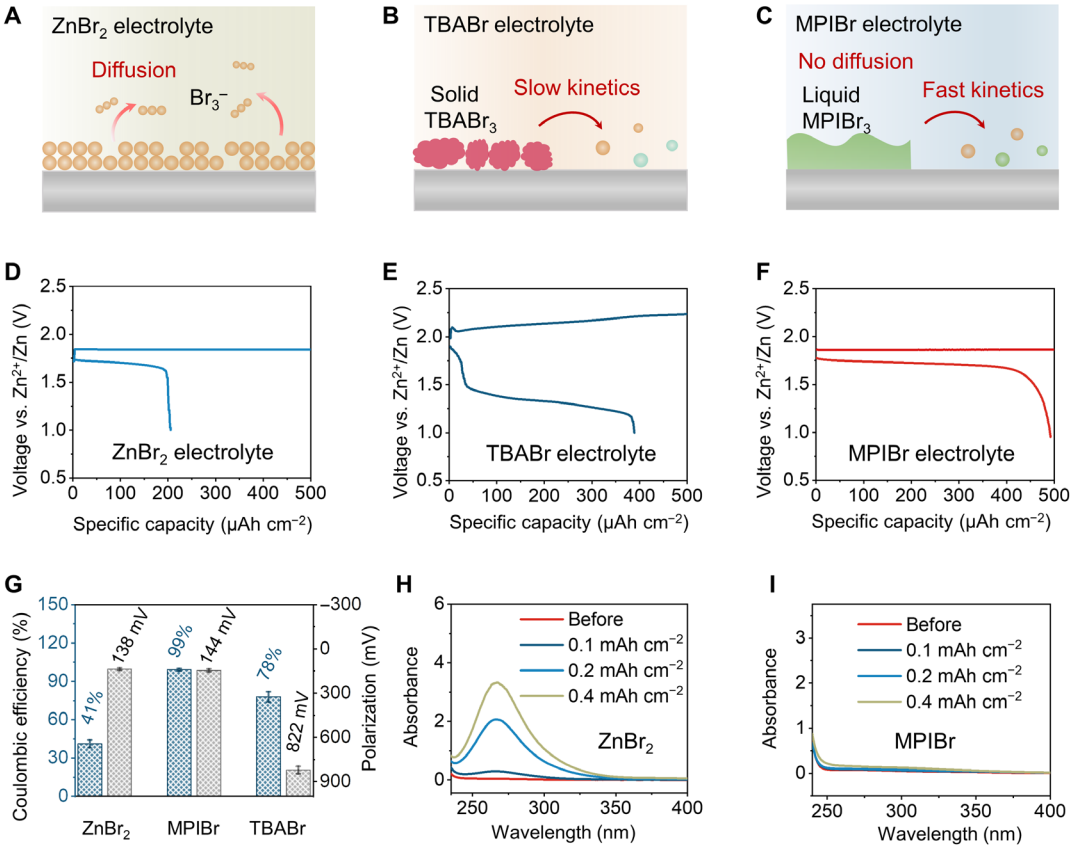

Fig. 2. Selection and optimization of the electrolyte. (**A**) Schematic of the fast diffusion of Br_3^- from current collector when $ZnBr_2$ solution is used as the electrolyte. (**B**) When TBABr is used as the electrolyte, solid-state $TBABr_3$ complex is generated, which shows slow reaction kinetics. (**C**) When MPIBr is used as the electrolyte, the oily phase $MPIBr_3$ complex is formed, which not only prevents the Br_3^- from dissolving into the electrolyte but also shows fast reaction kinetics. GCD curves of Zn-Br_2 batteries with (**D**) $ZnBr_2$, (**E**) TBABr, and (**F**) MPIBr electrolytes. These cells are tested in the homemade cells at 1 mA cm^{-2}. (**G**) The Coulombic efficiency and polarization comparisons of Zn-Br_2 batteries with different electrolytes. Error bars represent the SD of five independent batteries. UV-vis spectra of (**H**) $ZnBr_2$ and (**I**) MPIBr electrolytes after charging to 0.1, 0.2, and 0.4 mAh cm^{-2}.

the solution immediately becomes turbid (figs. S14 and S15 and movie S1), suggesting that MPI^+ and TBA^+ could form insoluble complex compounds with Br_3^-. In contrast, no change is noticed when $ZnBr_2$ is added to the solution (fig. S16).

Meanwhile, the concentration of Br^- in the electrolyte also affects the electrochemical performance of the Zn-Br_2 MBs. The electrolyte with 1.5 M MPIBr + 1.5 M $ZnSO_4$ shows the fastest plating rate (fig. S17), and a further increase to 2.0 M leads to incomplete dissolution of MPIBr (fig. S18). Therefore, unless otherwise specified, the electrolyte with 1.5 M MPIBr + 1.5 M $ZnSO_4$ is used in the following electrochemical tests.

Theoretical understanding of the advantages of MPIBr

To uncover the origins of high Coulombic efficiency and fast kinetics of MPIBr, first-principle calculations are performed. Here, the key issue is to compare the binding energy of various bromides (such as MPIBr, $MPIBr_3$, TBABr, etc.) to hydration energy of Br^- and Br_3^-. The binding energy per Br in compound ABr_n is defined as

$$E_b(\mathrm{Br}, \mathrm{A\,Br}_n) = [E(\mathrm{A\,Br}_n - E(A) - n \times E(\mathrm{Br})]/n$$

where E_b and E represent the binding energy and energy, respectively. The binding energy of Br in various bromides is shown in Fig. 3A. Both binding energies of Br in $MPIBr_3$ (−3 eV) and $TBABr_3$ (−3.4 eV) are lower than that of $ZnBr_4$ (−2.6 eV), ensuring the preference of Br_2 to form $MPIBr_3$ or $TBABr_3$ in the charging process and accumulate on the positive electrode. In the meantime, these values are also lower than the hydration energy of Br_3^- (−2.91 eV), implying that both $MPIBr_3$ and $TBABr_3$ can retain Br_3^- from dissociation. For comparison, the binding energy of Br in $ZnBr_4$ is higher than the hydration energy of Br_3^-, leading to the observed low Coulombic efficiency of 44% in the $ZnBr_2$ battery system. Moreover, the difference between binding energy of Br in $MPIBr_3$ (−3 eV) and hydration energy of Br^- (−3.71 eV) is larger than the difference between $TBABr_3$ (−3.4 eV) and hydration energy of Br^- (−3.71 eV), suggesting that the driving force in the MPIBr system is larger than that in the TBABr, demonstrating the fast reaction kinetics in the MPIBr system.

Microstructure greatly affects the reaction kinetics. To investigate the possible assembling form of $MPIBr_3$ and $TBABr_3$, their chain configurations are established (Fig. 3B). $MPIBr_3$ and $TBABr_3$ are supposed to form chain structures, which further consist spatial networks, as they have lower binding energies than their separated form. For $MPIBr_3$, its quasi–one dimensional molecule chain leads to a relative loose network structure. In contrast, the $TBABr_3$ molecule features a tetrahedral symmetry and has multiple equivalent directions to

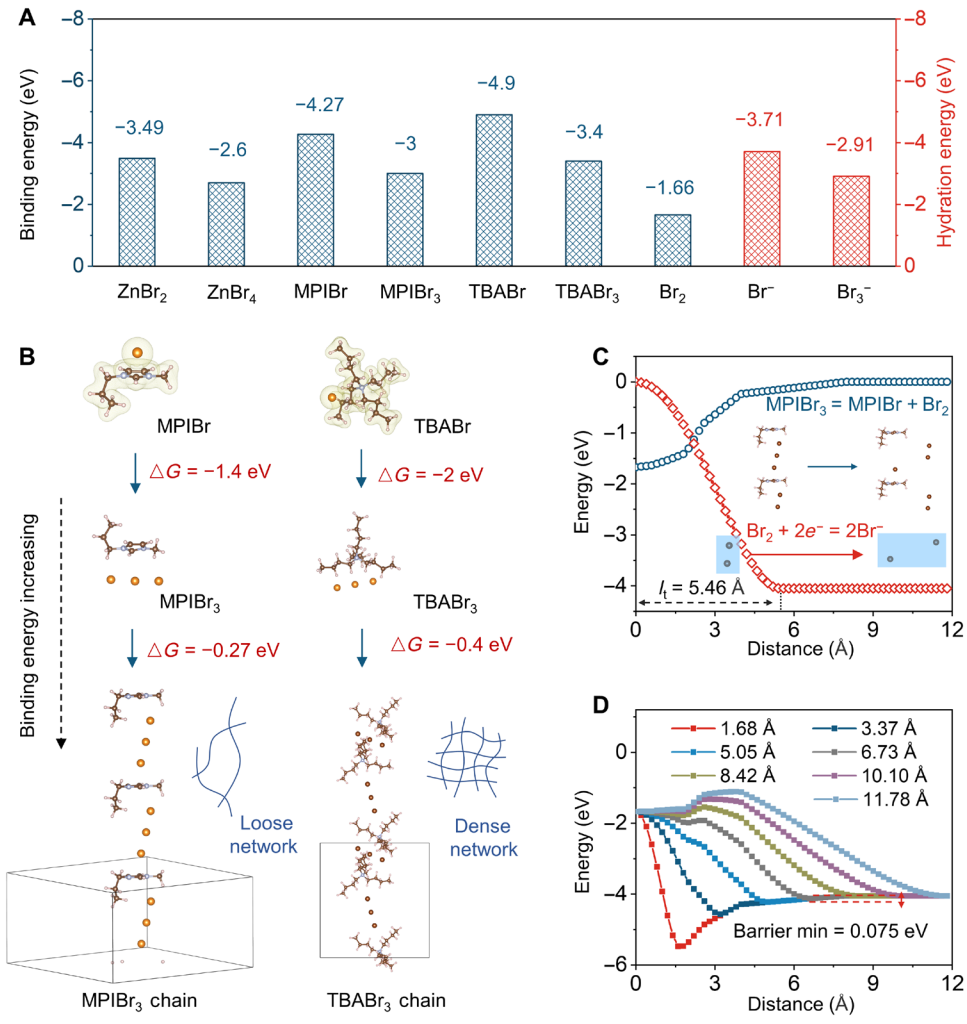

Fig. 3. Theoretical understanding. (**A**) Binding energy of Br in various bromides and hydration energy of Br^- and Br_3^-. (**B**) Relaxed molecule structures and binding process of the $MPIBr_n$ and $TBABr_n$ system. Chain configuration of $MPIBr_3$ and $TBABr_3$ is calculated and found to have a lower binding energy, suggesting that the network could be formed. According to structure feature, the loose network could be formed by $MPIBr_3$ chains, while the dense network could be formed by $TBABr_3$ chains (schematic diagram of networks are given and marked with blue color); C, brown; N, blue; H, pale pink; Br, yellow. (**C**) Energy variations of the two reactions ($MPIBr_3 = MPIBr + Br_2$ and $Br_2 + 2e^- = 2Br^-$) in discharging process. (**D**) Combination of these two reactions at different paces, which gives a notable energy barrier difference, and its minimum equals 0.075 eV.

continue its chain structure, which contributes to the eventual formation of a dense network. This configurational difference is also reflected by the fact that $MPIBr_3$ and $TBABr_3$ exist in liquid and solid states, respectively, and the loose network structure apparently endows the $MPIBr_3$ system with fast reaction kinetics.

The energy barrier is another factor to determine the reaction kinetics. To correctly estimate the energy barrier during the discharging process of $MPIBr_3$, the liquid form of $MPIBr_3$ should be considered. In this scenario, it is not necessary for Br_2 to be first dissociated from $MPIBr_3$ (i.e., $MPIBr_3 \rightarrow MPIBr + Br_2$) and then diffuse all the way to the interface for the reaction $Br_2 + 2e^- = 2Br^-$. With discharging process proceeding and the breakdown of the interfacial $MPIBr_3$ network, new interface could form at a short time due to its liquid form, which ensures fast reaction kinetics. Figure 3C shows the energy variation of the two reactions, and their combination at different paces is shown in Fig. 3D. Note that different l_t (the separated distance at the end of the reaction; see the Supplementary Materials for details) values are taken, and their corresponding energy curves are marked by different colors in Fig. 3D. The most possible combination in reality should be the one that gives minimum energy barrier, which is equal to 0.075 eV in terms of our calculation (details could be found in Materials and Methods). This ultralow energy barrier helps Zn-Br_2 MBs to realize extreme fast reaction kinetics.

Visualization of the dual-plating/stripping process

The in operando microscopy was used to study the dual-plating and dual-stripping working mechanisms of Zn-Br_2 MBs (Fig. 4A). Because it is hard to observe the $MPIBr_3$ complex on the black CNT microelectrode, here, Pt and Au wires (1 mm in diameter) were used as the positive and negative current collectors, respectively. Their smooth surface allows easy observation of the deposited electrodes. The Pt and Au wires both show a smooth and shiny surface before charging (Fig. 4B). Along with charging begins (0.1 mA cm^{-1}), lots of tiny yellow $MPIBr_3$ droplets appear and then gradually merge into larger

beads on the Pt surface, demonstrating the plating reaction of the $MPIBr_3$ cathode (Fig. 4, C to F) (*34*). Meanwhile, the glossy surface of a Au wire turns dark due to continuous Zn metal plating on it. The scanning electron microscopy images of the Au wire after charging for different times further demonstrate the gradual Zn plating process (fig. S19). The discharging procedure was performed after charging for 200 s, and the oily $MPIBr_3$ complex was stripped to Br^- and gradually decreased in size. The discharge ends at 1 V versus Zn^{2+}/Zn, and it lasts for 195 s. After discharging, the Au wire becomes shiny again, suggesting that almost all Zn metals have been stripped away. Meanwhile, there is only a little residual of $MPIBr_3$ complex on Pt (Fig. 4, G to K), demonstrating that the charging-discharging is reversible (Coulombic efficiency is 97.5%). The in operando visualization of the charging-discharging process (4 mA cm^{-2}) of Zn-Br_2 MBs based on the CNT paper microelectrode was also performed, where the plating and stripping processes of the zinc anode are quite clear (Fig. 4, L to P, and movie S2). The two in operando observations both demonstrate the dual-plating and dual-stripping working mechanisms of Zn-Br_2 MBs.

Electrochemical performance and flexibility of Zn-Br_2 MBs

The dual-plating strategy also endows the Zn-Br_2 MBs with excellent electrochemical performance. Figure 5A shows the cyclic voltammetry (CV) curves of the redox-active electrolyte in the three-electrode system, suggesting that the electrolyte could perform Br^-/Br_2 and Zn^{2+}/Zn redox reactions at the same time (*35*). Figure 5B shows the CV curves of the constructed Zn-Br_2 MBs, which is consistent with previously reported Zn-Br_2 batteries (*36*–*38*), suggesting the successful construction of Zn-Br_2 MBs through the dual-plating strategy.

The Zn-Br_2 MBs were constructed on the basis of the MPIBr gel electrolyte, which shows good ionic conductivity (3.4 S m^{-1}; fig. S20) and mechanical property (660% stretch ratio and 80% compression ratio; fig. S21). The Zn^{2+} transference number of the MPIBr gel electrolyte is 0.83 (fig. S22). The charging voltage strongly influences the electrochemical performance of the Zn-Br_2 MBs, and 1.85 V is applied during the charging process. A lower charging voltage (1.8 V) leads to a longer charging time, while a higher charging voltage (1.9 V) reduces the energy efficiency of Zn-Br_2 MBs (fig. S23). The discharging plateau is at about 1.7 V versus Zn^{2+}/Zn at 2 mA cm^{-2}. It shows an excellent rate performance, retaining about 72% capacity even at 20 mA cm^{-2} (Fig. 5C and fig. S24) and a maximum power density of about 26.2 mW cm^{-2} (fig. S25), further demonstrating the fast kinetics of the oily $MPIBr_3$ cathode. It shows a long shelf stability and slow self-discharging due to the inhibition of Br_3^- cross-diffusion (fig. S26). It also delivers a stable cycling performance for 1000 cycles at 5 mA cm^{-2} with a decay rate of 0.004% per cycle (Fig. 5D and fig. S27), which is the lowest value in the field of MBs (fig. S28). The positive current collector maintained its micromorphology after lone cycling (1000 cycles at 5 mA cm^{-2}) due to the liquid nature of $MPIBr_3$ (fig. S29). The maximum discharging areal capacity and energy density of Zn-Br_2 MBs are further studied. The Coulombic efficiency is more than 95% when charging capacity is less than 2000 μAh cm^{-2} (Fig. 5E and fig. S30). After charging to

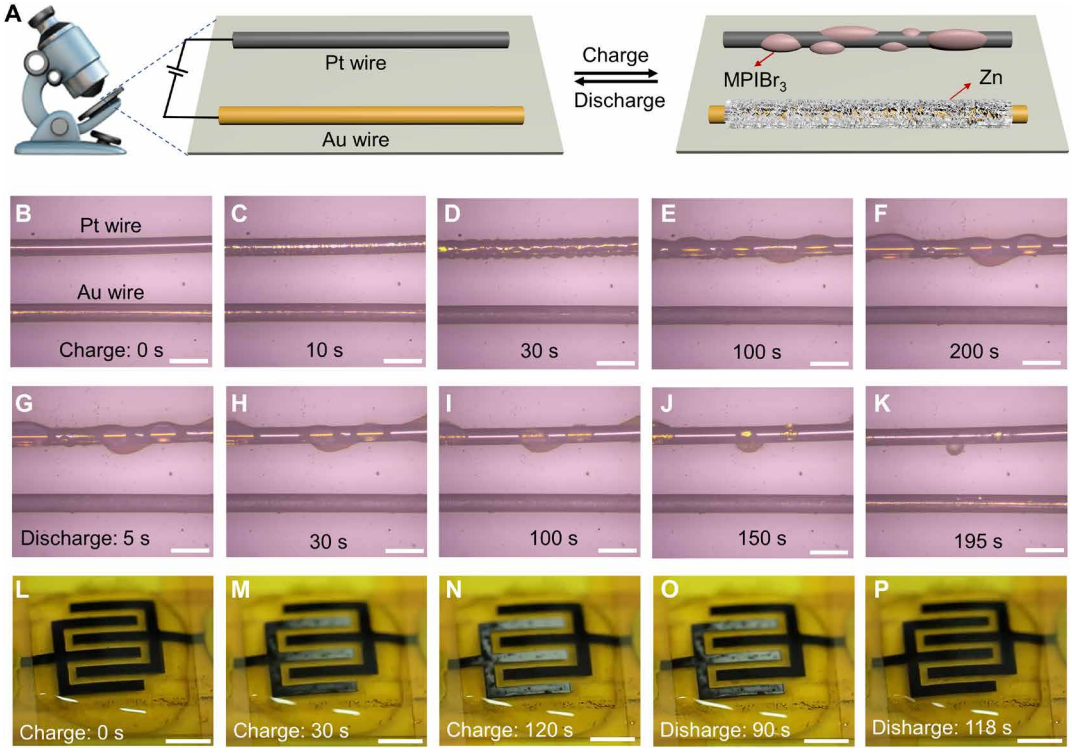

Fig. 4. In operando visualization of the charging-discharging process of Zn-Br_2 MBs. (**A**) Schematic of observation of the dual-plating process through the in operando microscope. The platinum (Pt) and gold (Au) wires are used as the positive and negative current collectors, respectively. (**B** to **F**) Time-lapse microscope images show oily $MPIBr_3$ complex that gradually forms on the Pt wire, and Zn generates on the Au wire during the charging process. (**G** to **K**) Time-lapse microscope images show oily $MPIBr_3$ complex on the Pt wire and Zn on the Au wire that gradually decrease during the discharging process. (**L** to **P**) The digital photographs show zinc plating and stripping processes of Zn-Br_2 MBs. Scale bars, 2 mm.

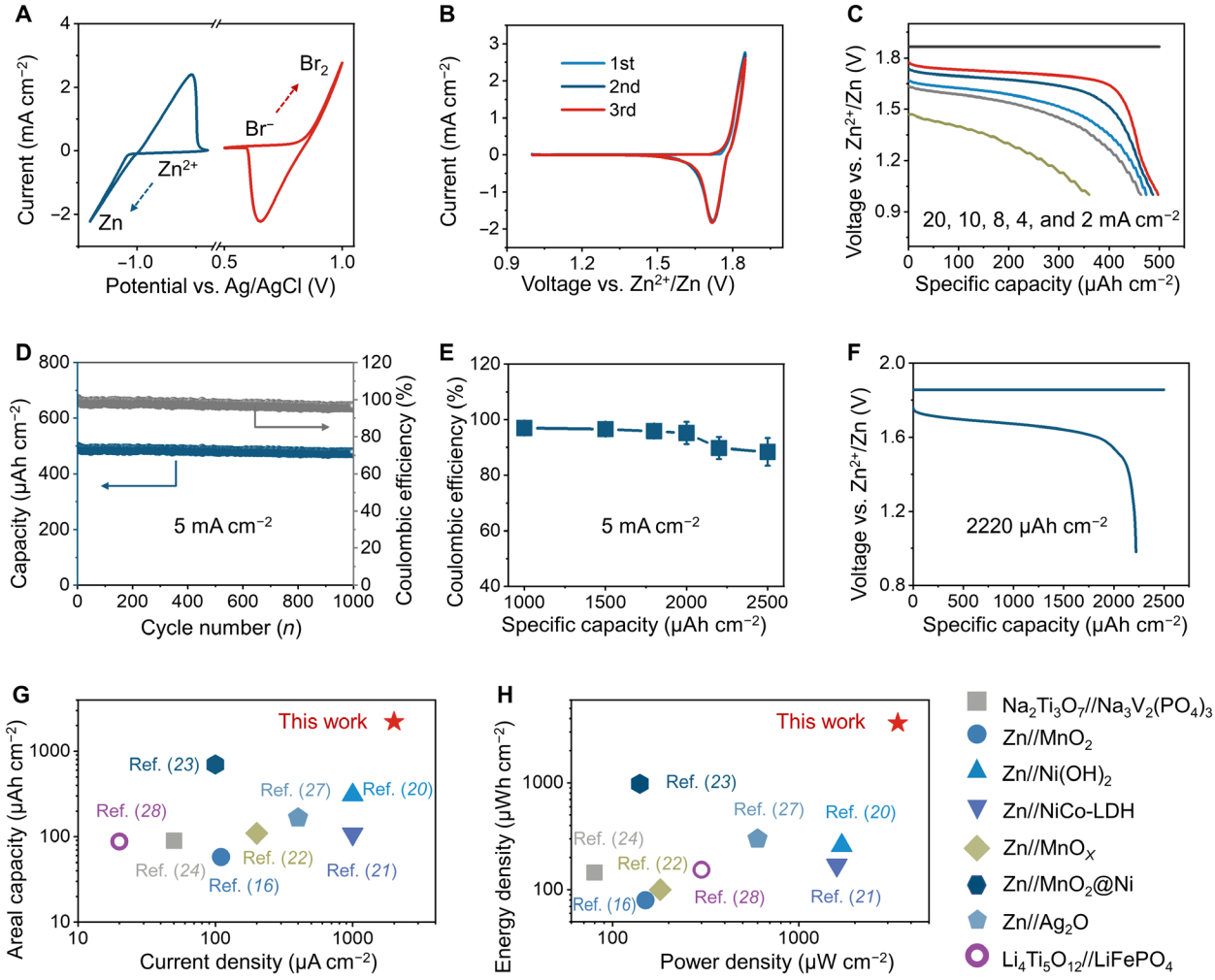

Fig. 5. Electrochemical performance of the Zn-Br_2 MBs. (**A**) CV curves of the redox-active electrolyte in a three-electrode system. (**B**) CV curves at 0.2 mV s^{-1}, (**C**) rate performance, (**D**) cycling performance, and (**E**) Coulombic efficiencies at different charge capacities. Error bars represent the SD of five independent batteries and (**F**) GCD curves at a charge capacity of 2500 μAh cm^{-2} of Zn-Br_2 MBs. Comparisons of (**G**) areal specific capacity and (**H**) areal energy density with other planar MBs.

2500 μAh cm^{-2}, the discharging areal capacity and energy density are up to record high values of 2220 μAh cm^{-2} and 3645 μWh cm^{-2} (Fig. 5F), respectively, which are even one magnitude higher than those of most reported planar MBs (Fig. 5, G and H; fig. S31; and table S1). It also shows high volumetric performance of 8 mAh cm^{-3} and 13.1 mWh cm^{-3} (based on the total volume of current collectors and gel electrolyte). Note that these high values are achieved under a considerably large current density and power density, further demonstrating the fast kinetics of the liquid cathode. It is worth mentioning that, unlike previous MBs with an excess of anode, the electrochemical data are obtained on the basis of the case of no electrode excess, which shows important implications for practical applications. As a proof of concept, a single Zn-Br_2 MB could power an electric fan and a red light-emitting diode (fig. S32).

The Zn-Br_2 MBs also show excellent flexibility as all of their components are highly flexible in nature (fig. S33). They deliver almost the same GCD curves under different bending angles (45°, 90°, and 180°), and they could suffer 1000 times bending without obvious changes (fig. S34, A to D). They also show a good cycling performance of 500 cycles at a bending angle of 180° (fig. S34E). The Zn-Br_2 MBs can be easily integrated to provide higher voltage or energy output (figs. S35 and S36). Three Zn-Br_2 MBs in series could deliver a 5.1-V voltage output, which could power most miniaturized electronic devices. The dual-plating strategy could also be extended to constructing Zn-I_2 and Zn-MnO_2 MBs (figs. S37 to S42).

Polarity-switchable function

Despite with the asymmetrical cathode and anode, the polarity of the Zn-Br_2 MB can be easily switched due to the dual-plating/stripping process. For a constructed Zn-Br_2 MB, the Br_2 cathode and the Zn anode completely change into soluble Br^- and Zn^{2+} and then dissolve into the electrolyte after discharging. The $MPIBr_3$ could deposit on the other current collector where Zn was previously plated once an opposite bias is applied, thus the cathode and anode of the microdevice are switched (Fig. 6A).

In operando technology could visualize such a process. The two microelectrodes are black before charging (Fig. 6B). The left one changes to white due to Zn anode deposition after charging at 1.85 V for 2 min (Fig. 6C), and it returns to black color after discharging to 0 V through CV at a scan rate of 5 mV s^{-1} (Fig. 6D). When the right

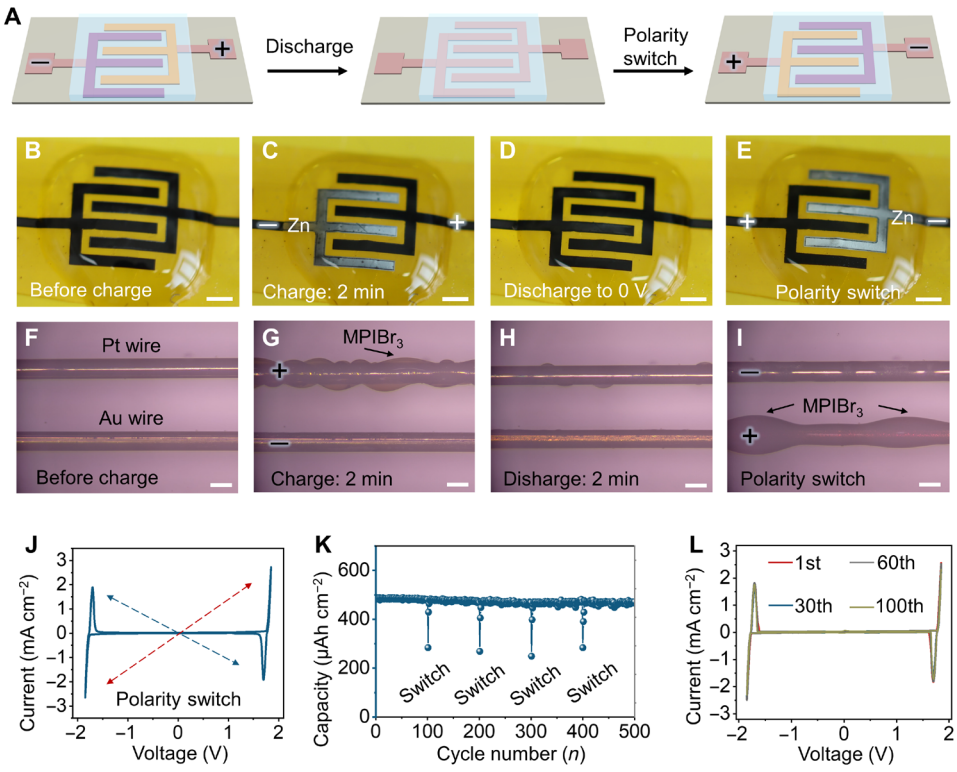

Fig. 6. Polarity-switchable capability of the Zn-Br_2 MBs. (**A**) Schematic and (**B** to **I**) in operando visualization of polarity-switchable process of Zn-Br_2 MBs. Scale bars, 1 mm. (**J**) CV curve of the polarity-switchable process. (**K**) Cycling performance of Zn-Br_2 MBs with the electrodes switched every 100 cycles. (**L**) CV curves of Zn-Br_2 MBs with repeatedly reversing the polarity for 100 cycles.

microelectrode is scanned from 0 to −1.85 V and held at −1.85 V for 2 min, it changes to white color (Fig. 6E), showing the polarity-switchable process. To clearly visualize the switch process of the $MPIBr_3$ cathode, the Pt and Au are used as the current collectors (Fig. 6F). The $MPIBr_3$ cathode is plated on the upper wire during the charging process (Fig. 6G), and it gradually disappears and lastly gets deposited on the lower wire with continuous discharging (Fig. 6, H to I, and movie S3).

The CV curves between −1.85 and 1.85 V show centrosymmetric features, further demonstrating the polarity switch of Zn-Br_2 MBs (Fig. 6J). The Zn-Br_2 MB could deliver a stable cycling performance of 500 cycles with switching cathode and anode every 100 cycles (Fig. 6K). Because a small portion of the $MPIBr_3$ cathode remains on the current collector during the GCD test, it reacts directly with the Zn anode when cathode and anode are switched, resulting in a lower discharging capacity with each polarity switch. It also could endure repeatedly reversing the polarity for 100 cycles (Fig. 6L and fig. S43), demonstrating that it could tolerate the misdeeming of cathode and anode, which usually results in complete damage or even safety issue in other batteries (*39*, *40*). Besides, the Zn-I_2 and Zn-MnO_2 constructed through the dual-plating strategy also have polarity-switchable functions (figs. S44 and S45). To the best of our knowledge, it is the first time that microscale energy storage devices show polarity-switchable functions.

DISCUSSION

In conclusion, we propose a dual-plating strategy to fast construct MBs with excellent electrochemical performance. This strategy eliminates complicated and time-consuming manufacture procedures of available MBs, bypasses the challenge of constructing and matching cathode and anode at a microscale, and enables the construction of liquid microelectrodes otherwise impossible by previous methods. We construct the first aqueous Zn-Br_2 MBs with a liquid cathode through using a novel redox-active MPIBr, which not only prevent diffusion of Br_3^- but also show fast kinetics during charging and discharging. The constructed Zn-Br_2 MBs show the zero excess of cathode and anode configuration and deliver a record high areal capacity and energy density (2.2 mAh cm^{-2} and 3.6 mWh cm^{-2}), more than 10 times of most planar MBs. The Zn-Br_2 MBs also show polarity-switchable capability, making them tolerate some wrong operations. This work offers new insights for constructing MBs and is promising to promote the development of miniaturized electronics.

MATERIALS AND METHODS

Materials

All materials, including free-standing CNT paper (Chengdu Organic Chemicals Co. Ltd., Chinese Academy of Sciences), MPIBr (99%; Meryer), $ZnSO_4$ (99.5%; Aladdin), $ZnBr_2$ (98%; Aladdin), TBABr (99.5%; Aladdin), $NaBrO_3$ (99.5%; Aladdin), HBr (AR, 40%; Aladdin), KBr (99%; Aladdin), 1-methyl-3-propylimidazolium iodide (MPII; $C_7H_{13}IN_2$, 99%; Meryer), $Mn(AC)_2{\cdot}4H_2O$ (99%; Tianjin Fucheng), $Zn(AC)_2{\cdot}2H_2O$ (99%; Tianjin Fucheng), acrylamide (99%; Acros Organics), ammonium persulfate (98%; Sigma-Aldrich), *N*,*N*′-methylenebisacrylamide (99%; Energy & Chemicals), and carbon cloth (Suzhou Wingrise Energy Technology Co. Ltd., HCP330N) are used without further purification.

Characterization of materials

The morphology and microstructure analysis of the synthesized materials were examined using field-emission scanning electron microscopy (Zeiss SUPRATM 55 SAPPHIRE) and transmission electron microscopy (FEI Tecnai TF20, USA). Raman spectra were performed by using a LabRAM HR Evolution (HORIBA Jobin Yvon, France) Raman microscope with a 532-nm laser. The UV-vis absorption spectrum was performed on a 2600-pc spectrophotometer. ^{1}H and ^{13}C NMR spectra were obtained using Bruker Avance III 400-MHz NMR Instruments. The high-resolution mass spectrometer was carried out on a Waters Xevo G2-XS time-of-flight mass spectrometer. The mechanical tensile tests of gel electrolytes were performed on a material testing system (Shimadzu AGS-X). Contact angle was measured by the contact angle measuring instrument (JC-2000CD).

Synthesis of quasi–solid-state redox-active electrolyte

Dry polyacrylamide (PAM) gel is first prepared. In a typical synthesis, 2.9 g of acrylamide monomer, 14.3 mg of ammonium persulfate, and 1.8 mg of *N*,*N*′-methylenebisacrylamide were added into 20 ml of deionized water. After stirring for 0.5 hours, the mixture was stored at 60°C for 12 hours to obtain the PAM hydrogel. Then, the PAM hydrogel was dried at 60°C for 12 hours to prepare dry PAM gel. The MPIBr gel electrolyte was obtained after immersing dry PAM gel in 1.5 M MPIBr + 1.5 M $ZnSO_4$ solution for 3 days. The MPIBr gel electrolyte film can be cut into the desired size for the Zn-Br_2 MB assembly. Each Zn-Br_2 MB uses about 50 μl of electrolyte. The MPII and $Mn(AC)_2$ gel electrolytes were prepared through immersing dry PAM in 0.5 M MPII + 0.5 M $ZnSO_4$ and 0.5 M $Mn(AC)_2$ + 0.5 $Zn(AC)_2$ solutions for 3 days, respectively.

Preparation of solution contains Br_3^- ions

The solution that contains Br_3^- was prepared through a previously reported method (*32*) and could be described as follows

$$NaBrO_3 + 5\,Br^- + 6\,H^+ \rightarrow 3\,Br_2(aq) + 3\,H_2O \quad (1)$$

$$Br_2(aq) + Br^- \rightleftharpoons Br_3^-(K\,eq = 16.1\,M^{-1}) \quad (2)$$

Typically, 5 ml of 2 M HBr, 5 ml of 2 M KBr, and 10 ml of 0.1 M $NaBrO_3$ were combined in a glass vial and stirred for 10 min to prepare 20 ml of solution that contains 120 mM Br_3^-, which shows dark orange.

Optimization of the electrolyte in homemade cell

The tests were performed in a homemade cell, as shown in fig. S2. The carbon cloth was used as the positive and negative current collectors (the distance between the two current collectors is about 1 cm), and about 1 ml of electrolytes (1 M $ZnBr_2$ or 0.1 M TBABr + 1 M $ZnSO_4$ or 1 M MPIBr + 1 M $ZnSO_4$) was used for different redox-active electrolytes. These cells were first charged at 1 mA cm^{-2} to 500 μAh cm^{-2} and then discharging at 1 mA cm^{-2} to 1 V.

Assembly of in-plane Zn-Br_2 MB

A flexible free-standing CNT paper (thickness of about 10 μm) was first pasted on the flexible polyimide tape. Then, the interdigital microelectrode was obtained through the laser engraving method. Each microelectrode is about 500 μm in width and 0.3 cm in length, and the distance between adjacent fingers is 300 μm. Last, a redox-active gel electrolyte was put on the microelectrode, and the polyimide tape was used for the packaging. The Zn-I_2 and Zn-MnO_2 MBs were constructed through the similar method but use MPII and $Mn(AC)_2$ gel electrolytes, respectively.

Ionic conductivity of MPIBr gel electrolyte

The ionic conductivity of MPIBr gel electrolyte is estimated on the basis of the following equation

$$\sigma = \frac{L}{R * S}$$

where σ (siemens per meter), L (meters), R (ohm), and S (square meters) are the ionic conductivity, thickness, ohmic resistance, and area, respectively. The ohmic resistance is from the electrochemical impedance spectroscopy (EIS) of Au/MPIBr gel electrolyte/Au cell.

Zn^{2+} transference number of MPIBr gel electrolyte

The Zn^{2+} transference number of the MPIBr gel electrolyte is estimated in Zn/MPIBr gel electrolyte/Zn cell based on the following equation (*41*)

$$t_{Zn^{2+}} = \frac{I_{SS}(\Delta V - I_0 R_0)}{I_0(\Delta V - I_{SS} R_{SS})}$$

where ΔV is the applied polarization voltage (10 mV), I_0 and R_0 are the initial current and interfacial resistance, and I_{SS} and R_{SS} are the steady-state current and interfacial resistance, respectively.

Calculation of energy efficiency

It is computed on the basis of

$$E = \frac{\int_0^{t_d} U_d I_d \, dt}{\int_0^{t_c} U_c I_c \, dt}$$

where E, t_d, U_d, and I_d are the energy efficiency, discharge time, discharge voltage, and discharge current, respectively; t_c, U_c, and I_c are the charge time, charge voltage, and charge current, respectively.

Electrochemical measurements

The optimization of the electrolyte was performed in a homemade cell, and the cells were galvanostatic cycled at 1 mA cm^{-2} on a LAND cycler (Wuhan Kingnuo Electronic Co., China). For the Zn-Br_2 MBs, these batteries were charged at 1.85 V to different areal capacities and then discharged at different current densities. The CV tests were recorded on a CHI 660e electrochemical workstation (Shanghai Chenhua, China) at a scanning rate of 1 mV s^{-1}. The areal performance was calculated on the basis of the total area of all fingers and gaps (0.18 cm^2). The volumetric performance is calculated on the basis of the total volume of current collectors and the gel electrolyte (50 μl). EIS was tested under an AC amplitude of 5 mV at the frequency from 100 kHz to 1 Hz under the open-circuit potential (constant potential). The recording number of data points was 12 (per decade). All electrochemical energy storage tests are carried out in an environmental chamber with a temperature of 25° ± 0.5°C.

First-principle calculations

The projector augmented wave pseudopotential method implemented in the Vienna Ab initio Simulation Package is used to perform

structural optimization and energy calculation (*42*). The energy cutoff and the electronic self-consistent step convergence are 400 and 10^{-5} eV, and the structure optimization ends when the total energy change between two steps is less than 0.01% of its total energy. Besides, the local density approximation exchange-correlation potential is applied for all calculations (*43*–*45*).

Barrier minimum estimation

The energy variation of $Br_2 + 2\ e^- = 2\ Br^-$ is described by

$$E(x) = \begin{cases} a x^2 + \frac{b}{2} x^4, x < l_t \\ -\frac{a^2}{2b}, x \geq l_t \end{cases}$$

where $a = 2\Delta E/l_t^2$ and $b = a/l_t^2$ are determined by the energy decrease ΔE (−4.05 eV) and separated distance l_t at the end of the reaction. Note that the energy decrease is obtained via first-principle calculation, while the separated distance is assumed. In Fig. 3C, l_t = 0.546 nm, and, in Fig. 3D, different values are taken for l_t to figure out the energy barrier minimum.

SUPPLEMENTARY MATERIALS

Supplementary material for this article is available at https://science.org/doi/10.1126/sciadv.abo6688

REFERENCES AND NOTES

1. P. Zhang, F. Wang, M. Yu, X. Zhuang, X. Feng, Two-dimensional materials for miniaturized energy storage devices: From individual devices to smart integrated systems. *Chem. Soc. Rev.* **47**, 7426–7451 (2018).
2. S. Zheng, X. Shi, P. Das, Z.-S. Wu, X. Bao, The road towards planar microbatteries and micro-supercapacitors: From 2D to 3D device geometries. *Adv. Mater.* **31**, 1900583 (2019).
3. N. A. Kyeremateng, T. Brousse, D. Pech, Microsupercapacitors as miniaturized energy-storage components for on-chip electronics. *Nat. Nanotechnol.* **12**, 7–15 (2017).
4. Y. Wang, Y. Zhao, L. Qu, Laser fabrication of functional micro-supercapacitors. *J. Energy Chem.* **59**, 642–665 (2021).
5. X. Jin, L. Song, C. Dai, Y. Xiao, Y. Han, X. Zhang, X. Li, C. Bai, J. Zhang, Y. Zhao, Z. Zhang, L. Jiang, L. Qu, An aqueous anti-freezing and heat-tolerant symmetric microsupercapacitor with 2.3 V output voltage. *Adv. Energy Mater.* **11**, 2101523 (2021).
6. K. Robert, D. Stiévenard, D. Deresmes, C. Douard, A. Iadecola, D. Troadec, P. Simon, N. Nuns, M. Marinova, M. Huvé, P. Roussel, T. Brousse, C. Lethien, Novel insights into the charge storage mechanism in pseudocapacitive vanadium nitride thick films for high-performance on-chip micro-supercapacitors. *Energ. Environ. Sci.* **13**, 949–957 (2020).
7. C. Gao, J. Huang, Y. Xiao, G. Zhang, C. Dai, Z. Li, Y. Zhao, L. Jiang, L. Qu, A seamlessly integrated device of micro-supercapacitor and wireless charging with ultrahigh energy density and capacitance. *Nat. Commun.* **12**, 2647 (2021).
8. G. Sun, H. Yang, G. Zhang, J. Gao, X. Jin, Y. Zhao, L. Jiang, L. Qu, A capacity recoverable zinc-ion micro-supercapacitor. *Energ. Environ. Sci.* **11**, 3367–3374 (2018).
9. X. Jin, G. Zhang, G. Sun, H. Yang, Y. Xiao, J. Gao, Z. Zhang, L. Jiang, L. Qu, Flexible and high-performance microsupercapacitors with wide temperature tolerance. *Nano Energy* **64**, 103938 (2019).
10. X. Li, Y. Wang, Y. Zhao, J. Zhang, L. Qu, Graphene materials for miniaturized energy harvest and storage devices. *Small Structures* **3**, 2100124 (2022).
11. J. Gao, C. Shao, S. Shao, F. Wan, C. Gao, Y. Zhao, L. Jiang, L. Qu, Laser-assisted large-scale fabrication of all-solid-state asymmetrical micro-supercapacitor array. *Small* **14**, 1801809 (2018).
12. B. Lu, F. Liu, G. Sun, J. Gao, T. Xu, Y. Xiao, C. Shao, X. Jin, H. Yang, Y. Zhao, Z. Zhang, L. Jiang, L. Qu, Compact assembly and programmable integration of supercapacitors. *Adv. Mater.* **32**, 1907005 (2019).
13. B. Lu, X. Jin, Q. Han, L. Qu, Planar graphene-based microsupercapacitors. *Small* **17**, 2006827 (2021).
14. Y. Han, C. Dai, J. Lin, F. Liu, H. Ma, Y. Wang, B. Lu, C. Shao, Q. Guo, X. Jin, X. Zhang, Z. Zhang, A compact aqueous K-ion micro-battery by a self-shrinkage assembly strategy. *Chem. Eng. J.* **429**, 132291 (2022).
15. S. Zheng, Z.-S. Wu, F. Zhou, X. Wang, J. Ma, C. Liu, Y.-B. He, X. Bao, All-solid-state planar integrated lithium ion micro-batteries with extraordinary flexibility and high-temperature performance. *Nano Energy* **51**, 613–620 (2018).
16. G. Sun, X. Jin, H. Yang, J. Gao, L. Qu, An aqueous Zn-MnO_2 rechargeable microbattery. *J. Mater. Chem. A* **6**, 10926–10931 (2018).
17. W. Lai, Y. Wang, Z. Lei, R. Wang, Z. Lin, C.-P. Wong, F. Kang, C. Yang, High performance, environmentally benign and integratable Zn//MnO_2 microbatteries. *J. Mater. Chem. A* **6**, 3933–3940 (2018).
18. Q. Liu, G. Zhang, N. Chen, X. Feng, C. Wang, J. Wang, X. Jin, L. Qu, The first flexible dual-ion microbattery demonstrates superior capacity and ultrahigh energy density: Small and powerful. *Adv. Funct. Mater.* **30**, 2002086 (2020).
19. Z.-S. Wu, X. Bao, C. Sun, S. Wang, X. Shi, J. Qin, F. Zhou, S. Zheng, X. Wang, Scalable fabrication of printed Zn//MnO_2 planar micro-batteries with high volumetric energy density and exceptional safety. *Natl. Sci. Rev.* **7**, 64–72 (2020).
20. Z. Hao, L. Xu, Q. Liu, W. Yang, X. Liao, J. Meng, X. Hong, L. He, L. Mai, On-chip Ni-Zn microbattery based on hierarchical ordered porous Ni@$Ni(OH)_2$ microelectrode with ultrafast ion and electron transport kinetics. *Adv. Funct. Mater.* **29**, 1808470 (2019).
21. Y. Wang, X. Hong, Y. Guo, Y. Zhao, X. Liao, X. Liu, Q. Li, L. He, L. Mai, Wearable textile-based Co-Zn alkaline microbattery with high energy density and excellent reliability. *Small* **16**, 2000293 (2020).
22. M. Zhu, Z. Wang, H. Li, Y. Xiong, Z. Liu, Z. Tang, Y. Huang, A. L. Rogach, C. Zhi, Light-permeable, photoluminescent microbatteries embedded in the color filter of a screen. *Energ. Environ. Sci.* **11**, 2414–2422 (2018).
23. B. He, Q. Zhang, L. Li, J. Sun, P. Man, Z. Zhou, Q. Li, J. Guo, L. Xie, C. Li, X. Wang, J. Zhao, T. Zhang, Y. Yao, High-performance flexible all-solid-state aqueous rechargeable Zn-MnO_2 microbatteries integrated with wearable pressure sensors. *J. Mater. Chem. A* **6**, 14594–14601 (2018).
24. S. Zheng, H. Huang, Y. Dong, S. Wang, F. Zhou, J. Qin, C. Sun, Y. Yu, Z.-S. Wu, X. Bao, Ionogel-based sodium ion micro-batteries with a 3D Na-ion diffusion mechanism enable ultrahigh rate capability. *Energ. Environ. Sci.* **13**, 821–829 (2020).
25. H. Wang, R. Guo, H. Li, J. Wang, C. Du, X. Wang, Z. Zheng, 2D metal patterns transformed from 3D printed stamps for flexible Zn//MnO_2 in-plane micro-batteries. *Chem. Eng. J.* **429**, 132196 (2022).
26. Z. Tian, Z. Sun, Y. Shao, L. Gao, R. Huang, Y. Shao, R. B. Kaner, J. Sun, Ultrafast rechargeable Zn micro-batteries endowing a wearable solar charging system with high overall efficiency. *Energ. Environ. Sci.* **14**, 1602–1611 (2021).
27. S. Bi, F. Wan, S. Wang, S. Jia, J. Tian, Z. Niu, Flexible and tailorable quasi-solid-state rechargeable Ag/Zn microbatteries with high performance. *Carbon Energy* **3**, 167–175 (2021).
28. S. Zheng, H. Wang, P. Das, Y. Zhang, Y. Cao, J. Ma, S. F. Liu, Z. S. Wu, Multitasking MXene inks enable high-performance printable microelectrochemical energy storage devices for all-flexible self-powered integrated systems. *Adv. Mater.* **33**, 2005449 (2021).
29. J. J. Hong, L. Zhu, C. Chen, L. Tang, H. Jiang, B. Jin, T. C. Gallagher, Q. Guo, C. Fang, X. Ji, A dual plating battery with the iodine/$[ZnI_x(OH_2)_{4-x}]^{2-x}$ cathode. *Angew. Chem. Int. Ed. Engl.* **58**, 15910–15915 (2019).
30. C. Dai, L. Hu, X. Jin, Y. Zhao, L. Qu, The emerging of aqueous zinc-based dual electrolytic batteries. *Small* **17**, 2008043 (2021).
31. J. Noack, N. Roznyatovskaya, T. Herr, P. Fischer, The chemistry of redox-flow batteries. *Angew. Chem. Int. Ed. Engl.* **54**, 9776–9809 (2015).
32. B. Evanko, S. J. Yoo, S.-E. Chun, X. Wang, X. Ji, S. W. Boettcher, G. D. Stucky, Efficient charge storage in dual-redox electrochemical capacitors through reversible counterion-induced solid complexation. *J. Am. Chem. Soc.* **138**, 9373–9376 (2016).
33. S. J. Yoo, B. Evanko, X. Wang, M. Romelczyk, A. Taylor, X. Ji, S. W. Boettcher, G. D. Stucky, Fundamentally addressing bromine storage through reversible solid-state confinement in porous carbon electrodes: Design of a high-performance dual-redox electrochemical capacitor. *J. Am. Chem. Soc.* **139**, 9985–9993 (2017).
34. Y. Wu, P.-W. Huang, J. D. Howe, Y. Yan, J. Martinez, A. Marianchuk, Y. Zhang, H. Chen, N. Liu, In operando visualization of the electrochemical formation of liquid polybromide microdroplets. *Angew. Chem. Int. Ed. Engl.* **58**, 15228–15234 (2019).
35. L. Gao, Z. Li, Y. Zou, S. Yin, P. Peng, Y. Shao, X. Liang, A high-performance aqueous zinc-bromine static battery. *iScience* **23**, 101348 (2020).
36. X. Li, T. Li, P. Xu, C. Xie, Y. Zhang, X. Li, A complexing agent to enable a wide-temperature range bromine-based flow battery for stationary energy storage. *Adv. Funct. Mater.* **31**, 2100133 (2021).
37. J. H. Lee, Y. Byun, G. H. Jeong, C. Choi, J. Kwen, R. Kim, I. H. Kim, S. O. Kim, H. T. Kim, High-energy efficiency membraneless flowless Zn-Br battery: Utilizing the electrochemical-chemical growth of polybromides. *Adv. Mater.* **31**, 1904524 (2019).
38. X. Li, N. Li, Z. Huang, Z. Chen, Y. Zhao, G. Liang, Q. Yang, M. Li, Q. Huang, B. Dong, J. Fan, C. Zhi, Confining aqueous Zn-Br halide redox chemistry by $Ti_3C_2T_X$ MXene. *ACS Nano* **15**, 1718–1726 (2021).
39. G. Wang, F. Wang, P. Zhang, J. Zhang, T. Zhang, K. Mullen, X. Feng, Polarity-switchable symmetric graphite batteries with high energy and high power densities. *Adv. Mater.* **30**, 1802949 (2018).

40. D. Chao, R. DeBlock, C.-H. Lai, Q. Wei, B. Dunn, H. J. Fan, Amorphous VO_2: A pseudocapacitive platform for high-rate symmetric batteries. *Adv. Mater.* , 2103736 (2021).
41. L. Chen, W. Li, L.-Z. Fan, C.-W. Nan, Q. Zhang, Intercalated electrolyte with high transference number for dendrite-free solid-state lithium batteries. *Adv. Funct. Mater.* **29**, 1901047 (2019).
42. G. Kresse, J. Furthmüller, Efficient iterative schemes for ab initio total-energy calculations using a plane-wave basis set. *Phys. Rev. B* **54**, 11169–11186 (1996).
43. J. P. Perdew, W. Yue, Accurate and simple analytic representation of the electron-gas correlation energy. *Phys. Rev. B Condens. Matter* **45**, 13244–13249 (1992).
44. J. P. Perdew, E. R. McMullen, A. Zunger, Density-functional theory of the correlation energy in atoms and ions: A simple analytic model and a challenge. *Phys. Rev. A* **23**, 2785–2789 (1981).
45. D. M. Ce Perley, B. J. Alder, Ground state of the electron gas by a stochastic method. *Phys. Rev. Lett.* **45**, 566–569 (1980).
46. D. Lin, D. Rao, S. Chiovoloni, S. Wang, J. Q. Lu, Y. Li, Prototypical study of double-layered cathodes for aqueous rechargeable static Zn-I_2 batteries. *Nano Lett.* **21**, 4129–4135 (2021).
47. H. Yang, Y. Qiao, Z. Chang, H. Deng, P. He, H. Zhou, A metal-organic framework as a multifunctional ionic sieve membrane for long-life aqueous zinc-iodide batteries. *Adv. Mater.* **32**, e2004240 (2020).
48. X. Li, N. Li, Z. Huang, Z. Chen, G. Liang, Q. Yang, M. Li, Y. Zhao, L. Ma, B. Dong, Q. Huang, J. Fan, C. Zhi, Enhanced redox kinetics and duration of aqueous I_2/I(−) conversion chemistry by MXene confinement. *Adv. Mater.* **33**, e2006897 (2021).
49. G. Liang, F. Mo, H. Li, Z. Tang, Z. Liu, D. Wang, Q. Yang, L. Ma, C. Zhi, A universal principle to design reversible aqueous batteries based on deposition-dissolution mechanism. *Adv. Energy Mater.* **9**, 1901838 (2019).
50. C. Liu, X. Chi, Q. Han, Y. Liu, A high energy density aqueous battery achieved by dual dissolution/deposition reactions separated in acid-alkaline electrolyte. *Adv. Energy Mater.* **10**, 1903589 (2020).
51. C. Zhong, B. Liu, J. Ding, X. Liu, Y. Zhong, Y. Li, C. Sun, X. Han, Y. Deng, N. Zhao, W. Hu, Decoupling electrolytes towards stable and high-energy rechargeable aqueous zinc-manganese dioxide batteries. *Nat. Energy* **5**, 440–449 (2020).

Acknowledgments: We thank Analysis and Testing Center, Beijing Institute of Technology for material characterizations. **Funding:** We acknowledge financial supports from NSFC (nos. 21975027, 11972349, 11790292, 22035005, 52073159, 52022051, 22075165, and 22109009) and the Strategic Priority Research Program of the Chinese Academy of Sciences (no. XDB22040503).
Author contributions: L.Q. and Z.Z. led the team and supervised the experiments. C.D., H.C., Y.Z., Z.Z., L.J., and L.Q. conceived the idea. C.D., L.H., X.J., Y.W., R.W., and Y.X. prepared the materials and performed the electrochemical measurements. C.D., X.L., X.Z., L.S., and Y.H. performed the characterizations and analyzed the corresponding data. F.L. contributed to the theoretical calculations. All authors discussed the results and agreed on the submission of the manuscript. **Competing interests:** The authors declare that they have no competing interests. **Data and materials availability:** All data needed to evaluate the conclusions in the paper are present in the paper and/or the Supplementary Materials.

Submitted 18 February 2022
Accepted 26 May 2022
Published 13 July 2022
10.1126/sciadv.abo6688